








A Novel Survey for Young Substellar Objects with the W-band Filter. VII. Water-Bearing Objects in the Core of the Rho Ophiuchi Cloud Complex

TANVI SHARMA ¹, WEN PING CHEN ^{1,2}, BETH BILLER ³, LOÏC ALBERT ^{4,5},
BELINDA DAMIAN ^{6,7}, JESSY JOSE⁸, BHAVANA LALCHAND ¹, MICHAEL C. LIU ⁹,
AND YUMIKO OASA¹⁰

¹*Institute of Astronomy, National Central University, 300 Zhongda Road, Zhongli 32001 Taoyuan, Taiwan*

²*Department of Physics, National Central University, 300 Zhongda Road, Zhongli 32001 Taoyuan, Taiwan*

³*Institute for Astronomy, Royal Observatory, University of Edinburgh, Blackford Hill, Edinburgh EH93HJ, UK*

⁴*Institut Trottier de recherche sur les exoplanètes, Université de Montréal, Montréal, QC, H3C 3J7, Canada*

⁵*Département de physique, Université de Montréal, Montréal, QC, H3C 3J7, Canada*

⁶*SUPA, School of Physics & Astronomy, University of St Andrews, North Haugh, St Andrews, KY16 9SS, UK*

⁷*Department of Physics and Electronics, CHRIST (Deemed to be University), Hosur Road, Bengaluru 560029, India*

⁸*Department of Physics, Indian Institute of Science Education and Research Tirupati, Yerpedu, Tirupati - 517619, Andhra Pradesh, India*

⁹*Institute for Astronomy, University of Hawai'i, 2680 Woodlawn Drive, Honolulu HI 96822*

¹⁰*Faculty of Education / Graduate School of Science and Engineering, Saitama University 255, Shimo-Okubo, Sakura, Saitama 338-8570, Japan*

ABSTRACT

We present a study of very low-mass stars and brown dwarfs in the rich star-forming core of the Rho Ophiuchi cloud complex. The selection of the sample relies on detecting the inherent water absorption characteristic in young substellar objects. Of the 22 water-bearing candidates selected, 15 have a spectral type of M6 or later. Brown dwarf candidates too faint for membership determination by Gaia have their proper motions derived by deep-infrared images spanning six years. Astrometric analysis confirms 21/22 sources as members, one identified as a contaminant. Infrared colors and the spectral energy distribution of each water-bearing candidate are used to diagnose the mass, age, and possible existence of circumstellar dust. 15 sources exhibit evidence of disks in their spectral energy distributions, as late as in M8-type objects. Spectroscopy for bright candidates has confirmed one as an M8 member and verified two sources (with disks) exhibiting signatures of magnetospheric accretion.

Brown dwarfs (BDs) are often referred to as “failed stars” because they do not reach core temperatures high enough to sustain hydrogen fusion like stars. In terms of formation and evolution, BDs bridge the mass gap between stars and planets, i.e., between $\lesssim 0.07 M_{\odot}$ and $\lesssim 0.013 M_{\odot}$ corresponding to the hydrogen and deuterium burning limit, respectively (Kumar 1963; Burrows et al. 1997). Even though there are numerous observations, there is still a lack of clear understanding regarding their formation mechanism, though various scenarios have been proposed. For example, BDs could form via turbulent fragmentation of clouds (Padoan & Nordlund 2002; Bonnell et al. 2008; Bate 2012); i.e., they could form like stars. Or, they could form like planets via gravitational instability (Whitworth & Stamatellos 2006) within young stellar disks. Alternatively, Reipurth & Clarke (2001); Bate & Bonnell (2005) suggest an ejection scenario in which a protostellar core is expelled from a stellar cluster, thereby ceasing accretion to become a star.

So far the most widely acknowledged mechanism is that BDs form like low-mass stars, supported by observational evidence of disks and accretion (e.g., Jayawardhana et al. 2003; Natta et al. 2004; Scholz & Jayawardhana 2008). However, studies by Manara et al. (2015), Alcalá et al. (2017), and Betti et al. (2023) suggest more active accretion in younger substellar objects, whereas no such age effect is observed in the stellar sample. If so, there must be additional factors affecting substellar formation. It is thus desirable to study BDs versus low-mass stars to diagnose their possible differences in the earliest evolution.

Young BDs (i.e., with late M to early L spectral types) exhibit prominent absorption due to water molecules (Allers & Liu 2020). For even cooler objects (i.e., late L to T types), methane begins to dominate (Chiang & Chen 2015). Spectroscopic identification of these intrinsically faint objects is feasible only if a reliable list of substellar targets is available. Broadband photometric observations to recognize cool objects often lead to a large fraction of contaminants such as reddened background stars or active galaxies. An effective way is to detect molecule-bearing objects by on-off imaging with filters centered on water or methane bands. This work is a part of one such program, called the “W Band” survey using near-infrared photometry sensitive to the water absorption near $1.45 \mu\text{m}$ as a detection marker to identify young BDs in nearby star-forming regions. The technique and design of the custom-made water filter with implementation and test results are described in Allers & Liu (2020). Subsequent applications have been reported for Serpens South and Serpens Core (Jose et al. 2020; Dubber et al. 2021, 2023), for Perseus (Lalchand et al. 2022), and for σ Orionis (Damian et al. 2023). Here we present the identification and characterization of BD candidates in Rho Ophiuchi.

The Rho Ophiuchi cloud complex is a nearby star-forming region with filamentary structures (Loren 1989; Ladjelate et al. 2020) including L 1688, with the sub-cloud L 1688A being the most active in star formation (Wilking et al. 2008). The youth (Greene & Meyer 1995; Luhman & Rieke 1999, 0.3 Myr) and proximity (Ortiz-León et

al. 2017; Zucker et al. 2020, ~ 137.3 pc) makes it an optimal laboratory to investigate the evolutionary stages of stellar and substellar objects in their infancy. The complex has been the focus of ample studies of young stars, for the substellar population, from discovery (Luhman & Rieke 1999; Erickson et al. 2011; Alves de Oliveira et al. 2010; Ducourant et al. 2017; Esplin & Luhman 2020), to presence of disks around BDs (Testi et al. 2016; Cieza et al. 2019), to observations of accretion and outflows (Natta et al. 2006; Ngoc 2022).

This work focuses on the main core of the complex, i.e., L 1688A, using the W-filter to unveil embedded BD members possibly not reported before, for which spectroscopy has been taken for some bright candidates to confirm their BD nature or to detect accretion signature. We also analyzed the spectral energy distribution (SED) or infrared colors of each candidate to probe possible existence of circumstellar dust. Moreover, proper motions of candidates too faint for Gaia have been derived with deep infrared images to constrain the membership.

2. DATA ANALYSIS AND RESULTS

Figure 1 illustrates the extent of our studied region. Sec. 2.1 describes the W-band images used to identify BD candidates. Sec. 2.2 then reports how we used archival images to derive the proper motion of faint candidates in reference to the Gaia DR3 measurements of bright sources. The SED and color analyses with multiwavelength photometric data are presented in Sec. 2.3. Sec. 2.4 describes confirmation infrared spectroscopic observations.

2.1. *W-Band Imaging and Selection of Candidates*

We used imaging observations from WIRCam implementing the custom-made water band filter (i.e., W-band) mounted on the CFHT 3.6 m telescope. WIRCam covered a $\sim 20' \times 20'$ field of view with a pixel scale of $0''.3$ (Puget et al. 2004). The observations were carried out on 2016 March 18 and July 20, with each epoch having 4 images per filter in *J* (1.25 microns), *H* (1.65 microns), and *W* (1.45 microns) bands, constituting a total integration time of 80 s in the *J* and *H* bands, and 520 s in the *W* band. The images were processed by the I²wi pipeline. The photometry in *J* and *H* bands was calibrated to 2MASS. The W-band calibration was conducted according to the procedure described in Allers & Liu (2020). The WIRCAM images contained 313 sources.

To diagnose the possible water absorption, Allers & Liu (2020) introduces a reddening-insensitive index, referred to as the *Q* index, which serves as a proxy for the water absorption feature inherently present in young substellar objects. *Q* is defined as

$$Q = J - W + e(H - W), \quad (1)$$

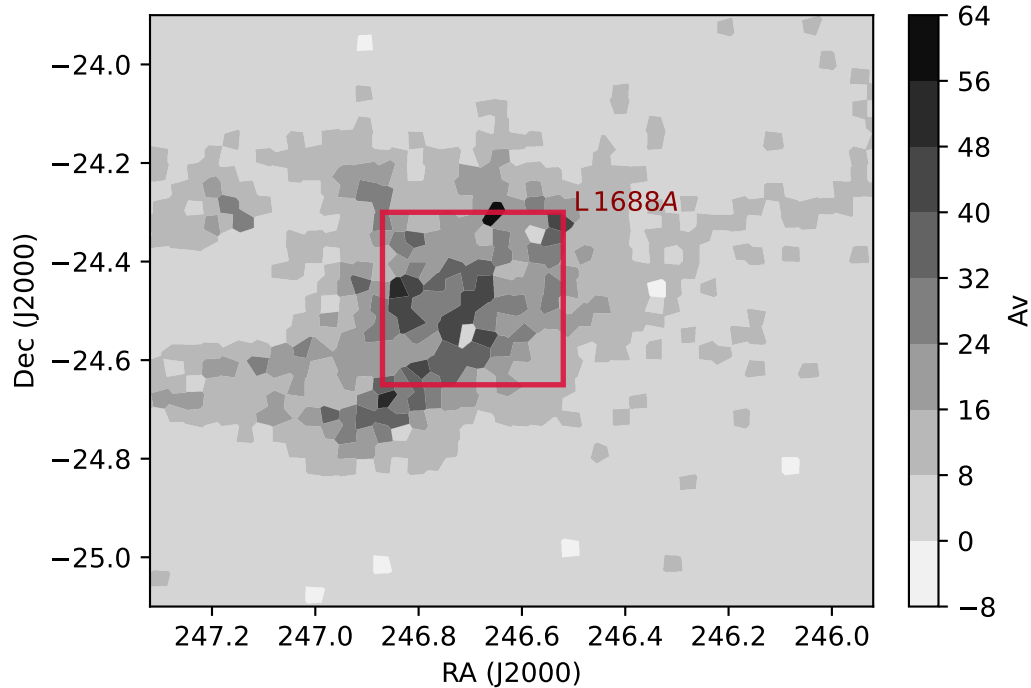


Figure 1. The spatial coverage of our study of L 1688A, with the underlying extinction map being computed using 2MASS catalog (Cutri et al. 2003) adopting the NICE technique from Lada et al. (1994). The color bar shows the extinction range. The red square encloses the area of the W band observations covering a field of $20' \times 20'$ corresponding to a linear scale of 0.8 pc.

where J , H , and W represent photometric data in their respective bands. The coefficient e is defined as

$$e = (A_J - A_W)/(A_W - A_H). \quad (2)$$

A_λ , the selective extinction in each filter (J , H , and W) derived by Allers & Liu (2020) using the spectrum of a M dwarf, its flux unreddened and reddened by $A_V = 10$ mag adopting the reddening law ($R_V = 3.1$) from Fitzpatrick (1999). We use their value of $e = 1.85$. The error in the Q index is derived by propagating photometric errors from the J , H , and W bands.

$$\sigma_Q = \sqrt{(\sigma_J^2 + (e\sigma_H)^2 + (1 + e)\sigma_W^2)}. \quad (3)$$

With no water absorption present in their spectra, typical field M dwarfs are expected to have $Q \approx 0$, and the value progressively decreasing to -0.6 for M6 type, and -1 for L0 types. Substellar candidates therefore are selected by (1) $Q < -(0.6 + \sigma_Q)$, i.e., for the water feature including the error, (2) $H \gtrsim 12$ mag to avoid saturation, and (3) $H \lesssim 16$ mag for reliable photometry; equivalently this corresponds to about an error $\lesssim 0.1$ mag in each band. The 19 Q candidates thus identified (Figure 2(a)) possess a Q value between -0.6 and -1.8 . There are two sources with a high negative

Q values (-3.5 and -9.3), and are not selected as per the criteria. Figure 2(b) labels sources with literature spectral types, namely by McClure et al. (2010); Esplin & Luhman (2020); Allers & Liu (2020), including 16 of our candidates. In addition, there are three sources, though fainter than $H = 16$ mag, included in our sample because they have $Q < 0.6$ with known spectral types of late M to L4. Figure 2 exhibits a general trend of Q varying with the spectral type and with the H mag for the low-mass objects and BDs in the cloud. Consequently, our final list consists of a total of 22 young BD candidates, whose coordinates, H band magnitude, Q values, and SIMBAD identifiers, are presented in Table 1, ordered by the spectral type.

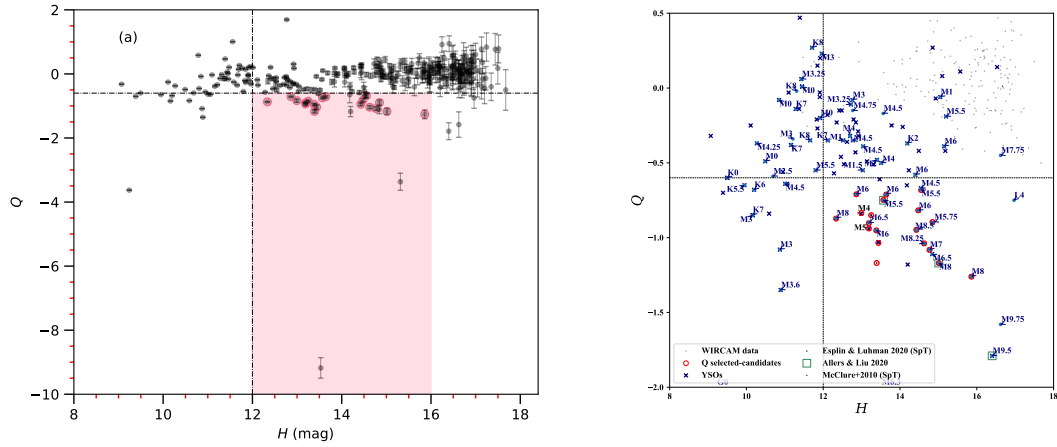


Figure 2. (a) The water Q index versus H mag for all WIRCam sources (in black). The Q candidates are marked in red. The pink shaded region highlights the region $Q < 0.6$ mag and H mag between 12 and 16. (b) The zoomed-in region around our candidates where spectral types in the literature if available are labeled.

Table 1. Water bearing BD candidates

No.	α (J2000)	δ (J2000)	SpTy	ref SpTy [†]	H (mag)	Q	Simbad identifier
1	246.76716	-24.47522	M4	1	13.08 (0.03)	-0.835 (0.049)	SSTc2d J162704.1-242830
2	246.60537	-24.41251	M5	1	13.10 (0.04)	-0.938 (0.037)	[GY92] 29
3	246.65755	-24.65098	M5.5	2	13.57 (0.04)	-0.747 (0.025)	SSTc2d J162637.8-243903
4	246.59925	-24.30808	M5.5	2	14.58 (0.06)	-0.682 (0.062)	SSTc2d J162623.8-241829
5	246.67014	-24.51427	M5.75	2	14.87 (0.06)	-0.895 (0.086)	SSTc2d J162640.8-243051
6	246.59567	-24.47951	M6	2	12.80 (0.02)	-1.082 (0.060)	SSTc2d J162622.3-242407
7	246.59248	-24.39787	M6	2	13.50 (0.03)	-0.712 (0.027)	[GY92] 10
8	246.57909	-24.40408	M6	2	13.75 (0.03)	-0.951 (0.025)	SSTc2d J162619.0-242414
9	246.63552	-24.44321	M6	2	14.46 (0.05)	-0.817 (0.052)	[GY92] 64
10	246.57842	-24.43637	M6.5	2	13.20 (0.03)	-0.904 (0.016)	SSTc2d J162618.8-242610
11	246.59275	-24.40192	M7	2	14.83 (0.01)	-1.082 (0.06)	SSTc2d J162622.3-242407
12	246.86070	-24.43190	M8	2	12.35 (0.02)	-0.872 (0.005)	SSTc2d J162726.6-242554
13	246.57738	-24.49771	M8	2	15.07 (0.01)	-1.170 (0.096)	SSTc2d J162618.6-242951
14	246.77472	-24.31119	M8	2	15.86 (0.02)	-1.260 (0.138)	SONYC RhoOph-6
15	246.71371	-24.54503	M8.5	2	14.47 (0.05)	-0.947 (0.044)	[RR90] Oph 2349.8-2601
16	246.51367	-24.50717	M9.5	2	16.45 (0.03)	-1.790 (0.260)	SONYC RhoOph-7
17	246.66634	-24.37600	M8.25	2	14.63 (0.04)	-1.038 (0.050)	[GY92] 90
18	246.85683	-24.62461	M9.75	2	16.60 (0.03)	-1.580 (0.400)	CFHTWIR-Oph 77
19	246.66536	-24.36837	L4	2	16.94 (0.04)	-0.750 (0.320)	CFHTWIR-Oph 33
20	246.77487	-24.43850	13.34 (0.03)	-1.034 (0.072)	YLW10A
21	246.70307	-24.63997	13.46 (0.00)	-0.850 (0.028)	BBRCG 8
22	246.62528	-24.64658	13.88 (0.20)	-1.169 (0.049)	...

[†] The reference for spectral types 1: [McClure et al. \(2010\)](#); 2: [Esplin & Luhman \(2020\)](#)

2.2. Multiepoch Astrometry and Motions

We further ascertained the membership of our young BD candidates by their motion. L 1688A has significant extinction, 50 mag or more in certain parts of the cloud (Figure 1), rendering Gaia data unavailable for the majority of our candidates. Lacking spectroscopically confirmed AGNs or QSOs in our field, we derived astrometry and hence proper motion of faint sources by using the CADC archives of deep WIRCam Ks-band images spanning six years from 2006 to 2012. The images for each epoch were stacked to generate a catalog of point sources using SExtractor (Bertin & Arnouts 1996). Gaia DR3 (Gaia Collaboration 2022) astrometry was exercised for calibration of bright sources to derive the motion of faint candidates, described below.

First, a group of “stationary” field objects were selected based on the Gaia proper motion. Figure 3(a) illustrates the segregation of cluster members from field stars. The field sample does not center at the origin as a result of the solar reflex motion. Near the center of this concentration at $(\mu_\alpha \cos \delta, \mu_\delta) = (-2.8, -3.7)$ mas yr⁻¹ are stars with null proper motion relative to the Sun. Next, within a radius of 1.5 mas yr⁻¹ of the center, we selected relatively bright Gaia stars (for which measurements are reliable) with nearly negligible parallax values and minimal errors (distant thereby with little expected proper motion). A total of 13 such high-confidence stationary Gaia objects are used to calibrate the astrometry with which to derive the proper motion in the deep infrared images.

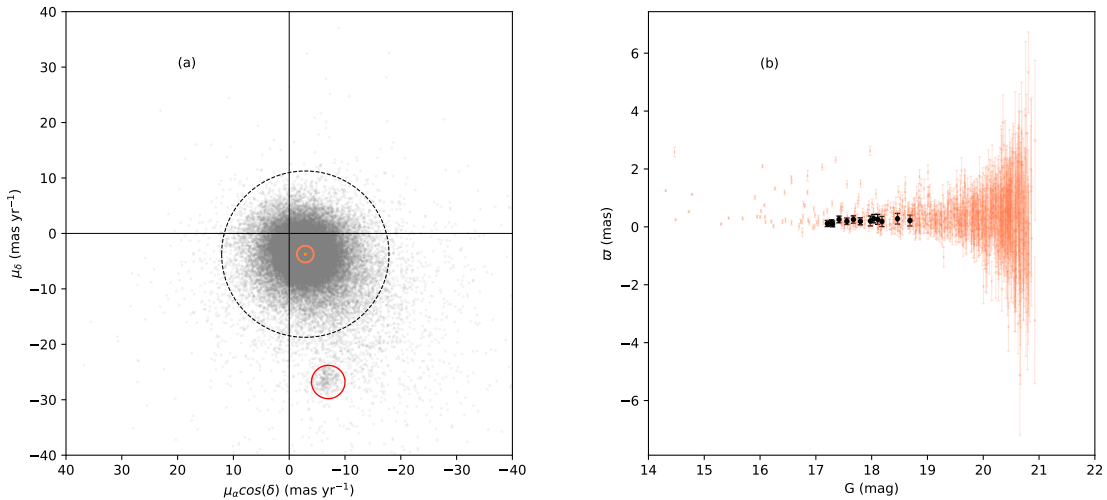


Figure 3. (a) Proper motion vector plot for Gaia DR3 sources. In addition to the L 1688A cluster in the lower right quadrant (red circle), the field population is concentrated. Stars inside the black dashed circle are used to compute a centroid sample, marked in orange, to represent “motionless” objects. (b) The parallax versus G band magnitude of the motionless objects selected in (a). Among these, 13 bright and distant objects, marked in black, are considered high-confidence stationary objects as proper motion standards.

We measured the device coordinates of all infrared sources relative to bright Gaia motionless standards, to derive proper motions between two epochs six years apart. The final value is the average of all 13 stationary objects, multiplied by the plate scale ($0''.3$), leading to proper motions in milliarcseconds per year (mas yr^{-1}).

Figure 4(a) exhibits the proper motion of sources derived from our images, including the YSOs compiled by [Esplin & Luhman \(2020\)](#) using motion from Spitzer’s multi-epoch observations, and those by [Grasser et al. \(2021\)](#) using Gaia data of known members to identify a large sample of new candidates. In this revised vector point diagram of proper motion, the data points are concentrated near the origin, denoting the field population, less the solar motion. In contrast, the motion of the YSOs with known motion clearly stands out, averaging $(\mu_\alpha \cos \delta, \mu_\delta) = (-6.7, -28.7) \text{ mas yr}^{-1}$ with standard deviations of $(\mu_\alpha \cos \delta, \mu_\delta) = (11.6, 12.4) \text{ mas yr}^{-1}$. Our 22 BD candidates, 3 of which have Gaia data and 13 with Spitzer measurements, have consistent kinematic distribution with those of the YSO samples. The kinematic membership of six (not in Gaia or Spitzer) are established in this work, five of which (sources No. 1, 2, 19, 20, 21) are associated with cluster, whereas (No. 22) is not. Figure 4(b) indicates that while our BD sample is fainter than Gaia, it still overlaps with brightness range covered by Spitzer’s. However, this analysis allowed us to derive, the proper motion of additional 161 young fainter candidates without prior information on kinematics from Gaia or Spitzer.

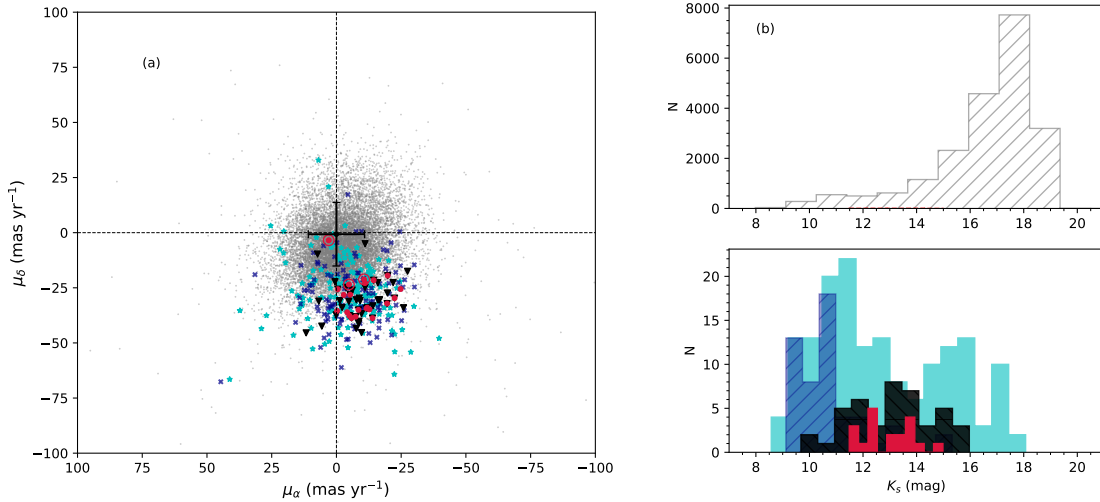


Figure 4. (a) All infrared sources (grey points) for which proper motions have been computed in this work, including our 22 BD candidates in red. Also marked are the 115 ([Grasser et al. 2021](#), Gaia, in blue) and 43 kinematic samples of YSOs ([Esplin & Luhman 2020](#), Spitzer, in black). The 161 candidates/members without previously reported proper motion are represented in cyan. The average of the motionless (field) sources is near $(0, 0)$ along with the corresponding dispersion (indicated in black). (b) The K_s mag distribution for, in the top panel, all infrared sources (grey), and, in the bottom panel, for young samples with the same color scheme as in (a)).

2.3. *Multiwavelength Archival Data and Dusty Disks*

To diagnose possible existence of dusty disks in the substellar objects, we have collected photometry for each source using VizieR photometry viewer (Allen et al. 2014) that includes optical from Pan-STARRS (Chambers et al. 2016), near-infrared from Two Micron All Sky Survey (2MASS) (Cutri et al. 2003), mid-infrared from Spitzer (Gunther et al. 2014) and WISE (Cutri & et al. 2012), far-infrared from Herschel (Herschel Point Source Catalogue Working Group et al. 2020), and ALMA 1.3 mm fluxes (Cieza et al. 2019) when available. The SEDs thus obtained is fit for each source with YSO models from Robitaille (2017), which for best results requires data points to have a minimum of five data points and sufficiently wide wavelength coverage, particularly in near-infrared and mid-infrared ranges which is available for 19 of our sources. The fitter treats both distance and extinction as free parameters. In our analysis we adopted a distance range of 120 pc to 150 pc, and an extinction between 0 and 40 mag. The SED and the best-fit model for each of the sources are presented in Figure 5. 15 Q selected objects show evidence of disks based on their SEDs.

Three sources (No. 19, 21, 22) lack data of sufficient wavelength coverage to render reliable SED fitting. For these, we inspected the color-color diagram (Figure 6), which serves as a simplified tool, though less robust than SEDs, to estimate possible infrared excesses originating from inner disks. Our color analyses reveals that one of the three candidates (i.e., No. 22) is devoid of infrared excess, appears to be a reddened giant star. No. 22 also exhibits an inconsistent proper motion, making it a contaminant in our BD sample. Overall, out of 22 candidates, 15 manifest dusty disks clearly evidenced by SEDs. Six sources exhibit near-infrared excess but lacks sufficient data at long wavelengths to be confirmed by SEDs leaving them to be disk candidates.

We also present a comparison of intrinsic colors of our BD sample with the dwarf locus in Figure 7. The dereddened colors for our sample are derived using extinction estimates from the SED fitting, and adopting the reddening law from Cohen et al. (1981). The extinction values and spectral type for M type members of the complex are taken from Esplin & Luhman (2020), which upon dereddening reproduces the dwarf locus of Bessell & Brett (1988) with an extension into classical T-Tauri region with near infrared excess. There is a continuous trend in the spectral type on locus of M dwarf down to the substellar regime. The alignment of Q candidates with the loci also suggests extinction from the SED fitting are reliable.

2.4. *Spectroscopic Observations*

We also acquired medium-resolution IR spectra of eight very low-mass and substellar objects using the SpeX instrument (Rayner et al. 2003) at Infrared Telescope Facility (IRTF). The observations were performed on 2023 August 3 and August 7. The short wavelength (0.25–2.5 μm) coverage in cross-dispersed mode with 0.8" slit was utilized to achieve a spectral resolution of 750. The K_s mag range of the targets was between

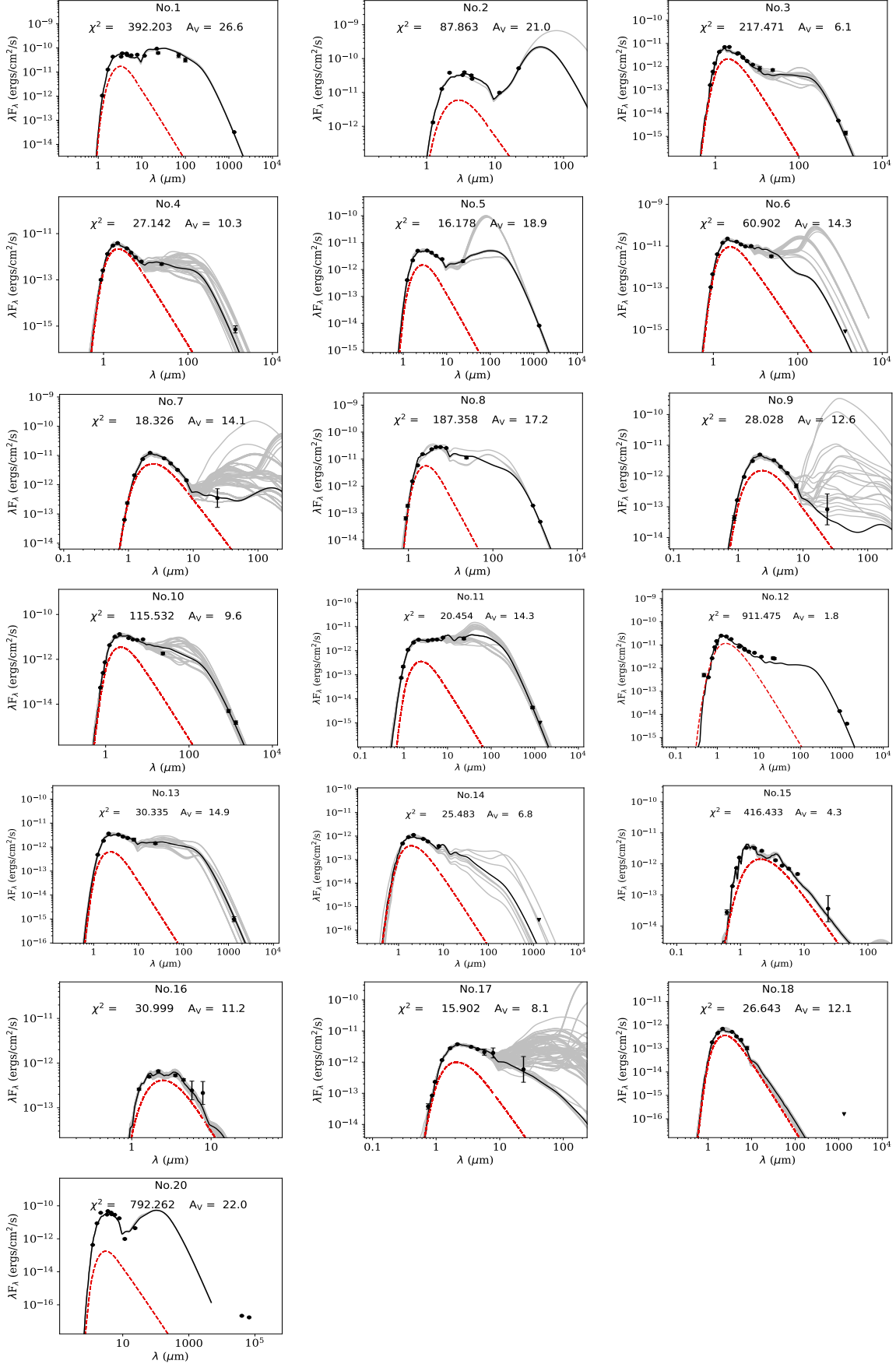


Figure 5. SEDs of all objects with the internal id from Table 1, and best fit parameters on each figure. The observed data points (N) are shown in black with best fit model curve in black, and in fairly good fit models with $\chi^2 - \chi^2_{min} < 3N$ is indicated in grey. The red dashed line represent the best fit blackbody curve.

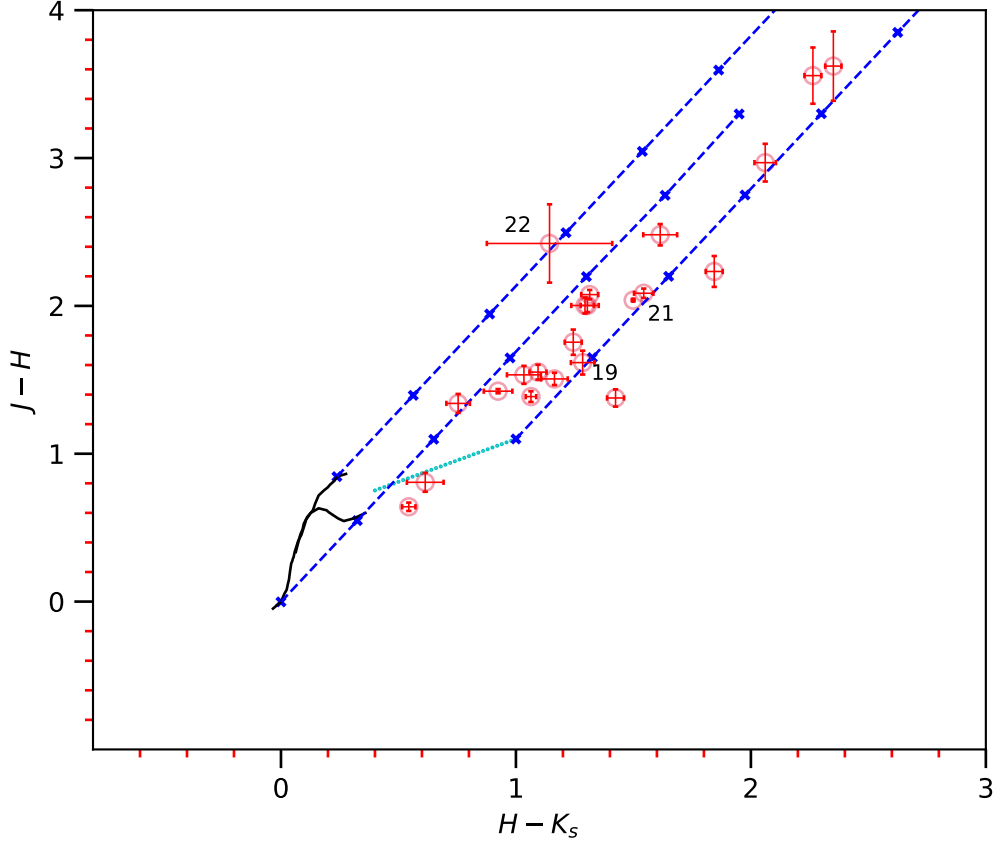


Figure 6. Near-infrared 2MASS $J - H$ versus $H - K_s$ color-color diagram. All of our Q candidates are marked by red circles, with the three sources not analyzed by the SEDs denoted by black squares, and are individually labeled. For reference, the black curves represent unreddened main sequence and giant star loci (Bessell & Brett 1988), whereas the intrinsic locus of classical T Tauri stars is represented by the cyan line (Meyer et al. 1997). The dashed blue lines indicate the direction of reddened objects along the reddening vector, adopting an interstellar law (Cohen et al. 1981), with blue crosses marked at intervals corresponding to A_V of 5 mag.

11 mag and 13.5 mag, with the integration time ranging from 1080 s to 1800 s. For telluric corrections, an A0V star (HD 147384) was observed throughout the observing run with an airmass < 0.1 and an angular separation < 5 deg from each science target. The data were reduced in the standard manner employing the reduction tool SpeXtool version 4.1 (Cushing et al. 2004; Vacca et al. 2003). The observing log is presented in Table 2.

Among the eight spectroscopic targets, four were Q selected candidates, and four were known substellar objects but outside the field of the W-band image. All but one (No. 20) have had spectral typing available in the literature. The purpose of the spectroscopy, in addition to ascertain the substellar nature, is to detect possible

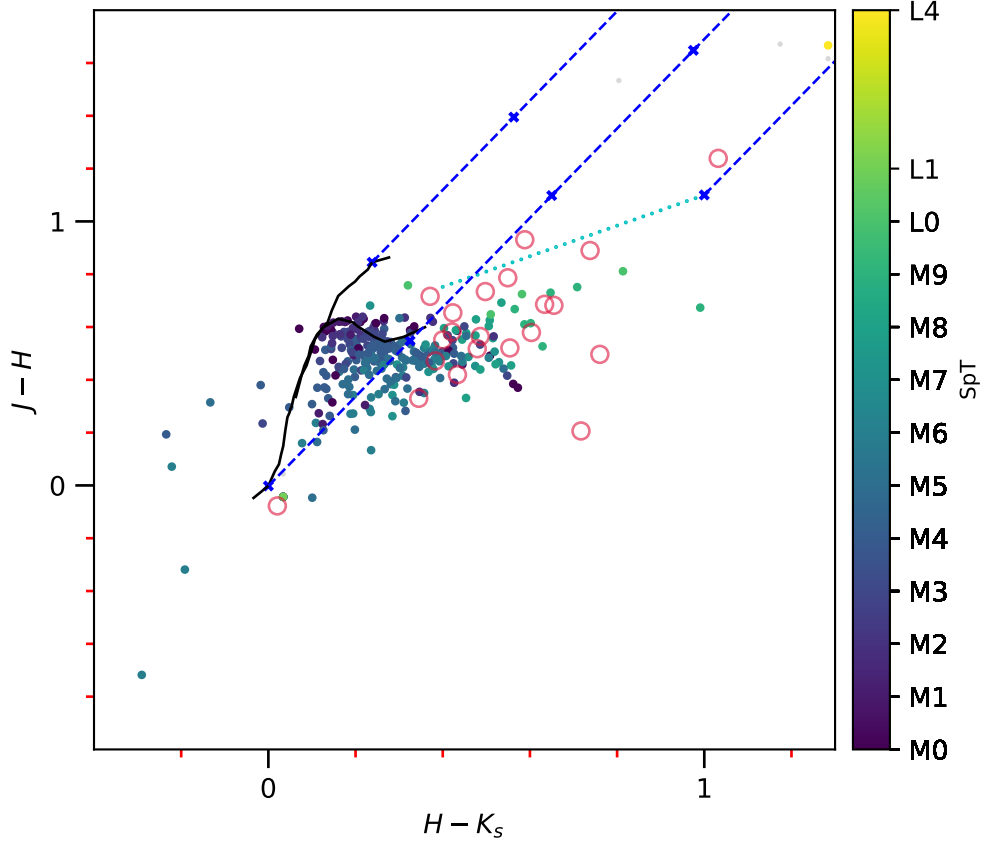


Figure 7. The same as in Figure 6 with Q candidates (red circles) and M dwarfs dereddened and color coded with respective spectral types.

Table 2. IRTF Observing log

No.	α (J2000)	δ (J2000)	SpT ^b	K_s	i time	Simbad identifier
				(mag)	(sec)	
8	246.63552	-24.44321	M6	11.9	1440	[GY92] 64
13	246.57738	-24.49771	M8	13.5	1200	BKLT J162848 242631
17	246.66634	-24.37600	M8.25	13.5	1800	[GY92] 90
20	246.77487	-24.43850	...	11.1	1080	YLW10A
23	247.05300	-24.19322	M6.25	11.1	1080	ISO Oph 193
24	247.20296	-24.44226	M6.25	13.1	1440	CFHTWIR Oph107
25	246.92016	-24.48366	M7.5	13.1	1440	[GY92] 320
26	246.76676	-24.04642	M7.25	13.2	1800	CFHTWIR Oph57

^a Source No. 8, 13, 17, 20 (upper panel) are water bearing candidates from Table 1. The remaining four (lower panel) are outside the field of W-Band imaging.

^b Spectral types from Esplin & Luhman (2020)

accretion features, such as $\text{Pa}\beta$ and $\text{Br}\gamma$ emission lines. The reduced spectra are

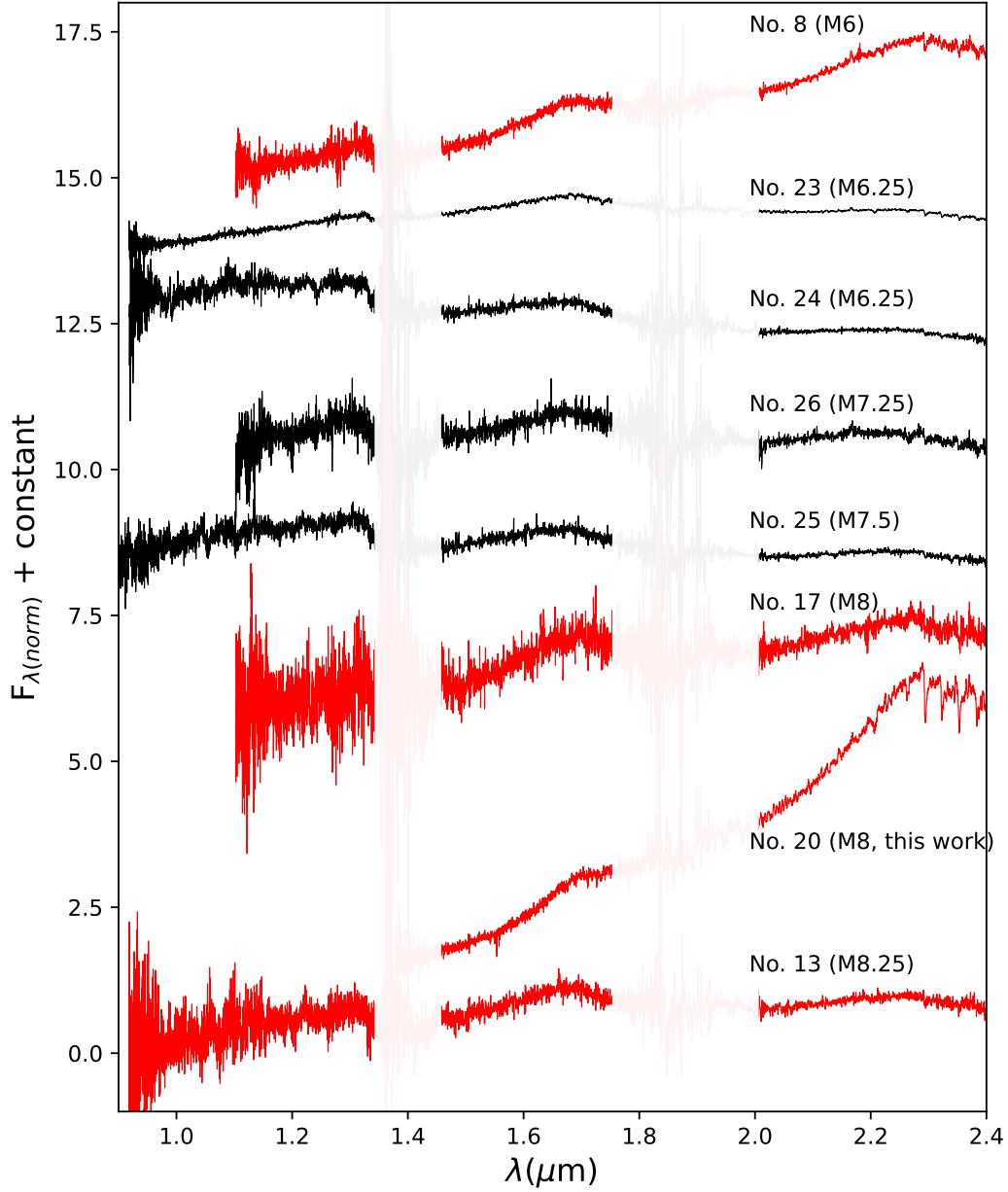


Figure 8. Reduced IRTF spectra of *Q* candidates (in red) and known low-mass objects outside the W-band image (in black), each with the source ID (as per Table 2) and spectral type labeled. No. 20 has poor data quality in the *J* band, so only the long-wavelength spectrum is shown.

exhibited in Figure 8, in order of the spectral type, with object No. 20 determined to be an M8.

The inverted-V shape near $1.67 \mu\text{m}$ in the spectra characteristic of young substellar nature (e.g., Lucas et al. 2001; Luhman et al. 2004; Kirkpatrick et al. 2006; Allers et al. 2007) can be seen in most targets, and more prominent for later spectral types. Figure 9 zooms in near the $\text{Pa}\beta$ and $\text{Br}\gamma$ lines where magnetospheric accretion shocks would produce these lines in emission.

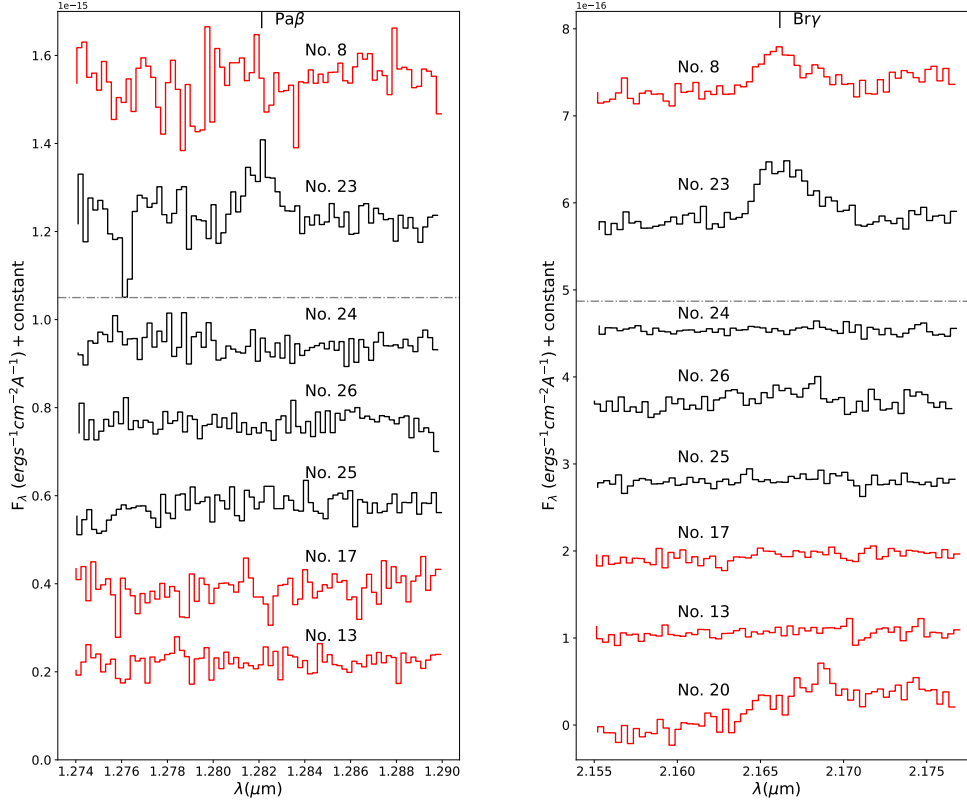


Figure 9. The same spectra as in Figure 8 but zoomed in to near $\text{Pa}\beta$ on the left panel and $\text{Br}\gamma$ on the right panel (less No. 20). Accretion features are detected in the top two sources, namely, No. 8 and No. 23.

Target No. 8 is known to have $\text{Pa}\beta$ (Natta et al. 2006), while No. 23 is known to have both $\text{Pa}\beta$ and $\text{Br}\gamma$ emission (Natta et al. 2006; Gatti et al. 2006). In our data, No. 23 displays clear emission indeed in $\text{Pa}\beta$ (Figure 9), with an EW of $1.86 \pm 1.39 \text{ \AA}$. However, in No. 8 $\text{Pa}\beta$ emission is not as clear, with the EW of $3.54 \pm 3.98 \text{ \AA}$. Both these measured values are consistent with the literature. Our spectra of both targets show clear evidence of accretion in $\text{Br}\gamma$. To our knowledge, our observations present the first $\text{Br}\gamma$ detection for No. 8. The equivalent width (EW) is determined by integrating the area under the line after subtracting the local continuum flux. Subsequently, the line flux (f_{line}) is calculated by multiplying the EW with the extinction-corrected

flux, using A_J and J for Pa β , and A_{K_s} and K_s for Br γ , where A_J and A_{K_s} represent the extinction in J and K_s bands. This line luminosity is then estimated by $4\pi d^2 f_{\text{line}}$ assuming a distance of 137.3 pc (Ortiz-León et al. 2017). The line luminosity is converted to accretion luminosity (Calvet et al. 2004; Natta et al. 2004). For non-detections, the 3σ upper limit on the EW is calculated as $3(\Delta f/f_{\text{ctn}})\Delta\lambda$, where Δf is the rms flux noise of each spectrum, f_{ctn} is the continuum flux, and adopting $\Delta\lambda$ equal to the linewidth of 40 Å. The corresponding accretion luminosity is calculated using the same methodology described for detected lines. The accretion luminosities from this work, and collected from literature (Natta et al. 2006; Manara et al. 2015; Almendros-Abad et al. 2024) are listed in Table 3.

Table 3 summarizes some properties of our Q candidates. A sequence number is assigned in Column 1, followed by the spectral type in Column 2. Column 3 and Column 4 then list the proper motions computed in this work. The dust masses estimated from the 1.3 mm fluxes (Testi et al. 2022) and from those obtained from SED fitting are presented in Column 5 and Column 6. Column 7 and Column 8 give the accretion luminosity derived from our IRTF observations, or gathered from the literature. The last column remarks on our membership assessment of each Q candidate. Four additional objects not within our W -band images therefore not as Q candidates, but have been spectroscopically observed to look for accretion signatures are separately summarized in Table 4.

Table 3. Youth and membership of water bearing BDs

No.	SpTy	μ_α (CFHT-K _S)	μ_δ (CFHT-K _S)	M_{Disk} (1.3mm)	M_{Disk} (SED)	$\log(L_{acc}/L_\odot)$	$\log(L_{acc}/L_\odot)$	ref L_{acc}	Membership
		mas yr ⁻¹	mas yr ⁻¹	M_\oplus	M_\oplus	(this work, IRTF)	(literature)		
1	M4	-4.14	-36.07	8.29	64.60	...	< -2.18	3	Y
2	M5	-2.82	-28.22	...	1.65	...	< -3.36	3	Y
3	M5.5	-11.06	-22.84	0.37	3.16	...	< -4.4	4	Y
4	M5.5	-5.33	-28.16	0.2	0.51	...	< -4.4	4	Y
5	M5.75	-19.57	-32.15	2.1	33.96	...	< -4.02	3	Y
6	M6	-14.38	-21.56	0.21	1.03	Y
7	M6	-13.94	-38.76	...	0.01	Y
8	M6	-19.78	-19.46	12.4	148.52	-1.48 ± 0.13	-1.8	3	Y
9	M6	-7.41	-38.09	Y
10	M6.5	-8.5	-35.01	0.4	4.86	...	-3.65	3	Y
11	M7	-11.92	-34.03	0.26	0.05	...	< -5.82	3	Y
12	M8	-12.78	-34.8	1.0	0.01	...	< -4.1	4	Y
13	M8	-4.96	-37.59	0.26	0.16	< -3.35	Y
14	M8	-22.46	-29.67	0.07	< -4.1	4	Y
15	M8.5	-24.77	-25.54	0.07	Y
16	M9.5	-5.83	-38.71	Y
17	M8.25	-0.54	-25.63	...	0.01	< -3.60	Y
18	M9.75	-11.62	-34.33	0.04	< -3.9	4	Y
19	L4	-0.26	-35.45	Y
20	M8 (this work)	-10.67	-21.21	...	1.78	< -2.56	Y
21	...	-4.82	-23.48	Y
22	...	2.99	-3.44	N

^a The same source ID number in Column 1 as in table 1

[†]The reference for accretion luminosity 3: Manara et al. (2015), 4: Almindros-Abad et al. (2024)

Table 4. Additional Targets with IRTF Spectra

No.	α (J2000)	δ (J2000)	SpT	$\log(L_{acc}/L_{\odot})$ (this work)
23	247.053	-24.19322	M6.25	-1.83 ± 0.32
24	247.20296	-24.44226	M6.25	< -3.94
25	246.92016	-24.48366	M7.5	< -3.75
26	246.76676	-24.04642	M7.25	< -3.51

3. DISCUSSION

3.1. Masses and Ages

The mass and age are characterised by using HR diagram and isochrones. The effective temperature is converted from the spectral type adopting the relations from [Herczeg & Hillenbrand \(2015\)](#) for those earlier than M7, and from [Filippazzo et al. \(2015\)](#) for later types. The bolometric luminosity is derived from J mag with the bolometric correction from [Herczeg & Hillenbrand \(2015\)](#) and [Filippazzo et al. \(2015\)](#). A distance of 137.3 pc ([Ortiz-León et al. 2017](#)) is adopted to calculate the luminosity, along with interstellar extinction derived from the SED fitting whenever available. Otherwise A_V is taken from the literature. The effective temperature versus bolometric luminosity is then compared with theoretical isochrones, as depicted in [Figure 10](#).

The majority of our sources have masses less than $0.08 M_{\odot}$, and ages younger than 5 Myr; some are very low mass stars near the hydrogen burning limit, and many are BDs well within the substellar regime. The objects with detected accretion span the mass range of $0.08 M_{\odot}$ to $0.06 M_{\odot}$. Most of our sources are confined near the isochrones, except YLW10A, which will be discussed later in detail.

3.2. Disks and Accretion

Disks around low mass stars and BDs provide insights into (a) planet formation (b) youth and evolutionary status (c) substellar formation pathway.

While direct observations of planet formation in BD disks are lacking, indirect evidence such as grain settling ([Apai et al. 2005](#)) has been observed in BD disks, indicating the potential for planet formation. With the presence of disk and estimation of disk masses, the upper limit on the mass and size of the planet to be formed can be inferred. In our sample, the disk dust mass obtained from the SED fitting has a median of $1.34 M_{\oplus}$, higher than those available from continuum fluxes at 1.3 mm ([Cieza et al. 2019](#); [Testi et al. 2022](#)), are listed in [Table 3](#)). Assuming a gas to dust ratio of 100, this total disk mass corresponds to $134 M_{\oplus}$, or equivalently $0.4 M_J$. It appears that with such low disk masses, the available material is not enough to

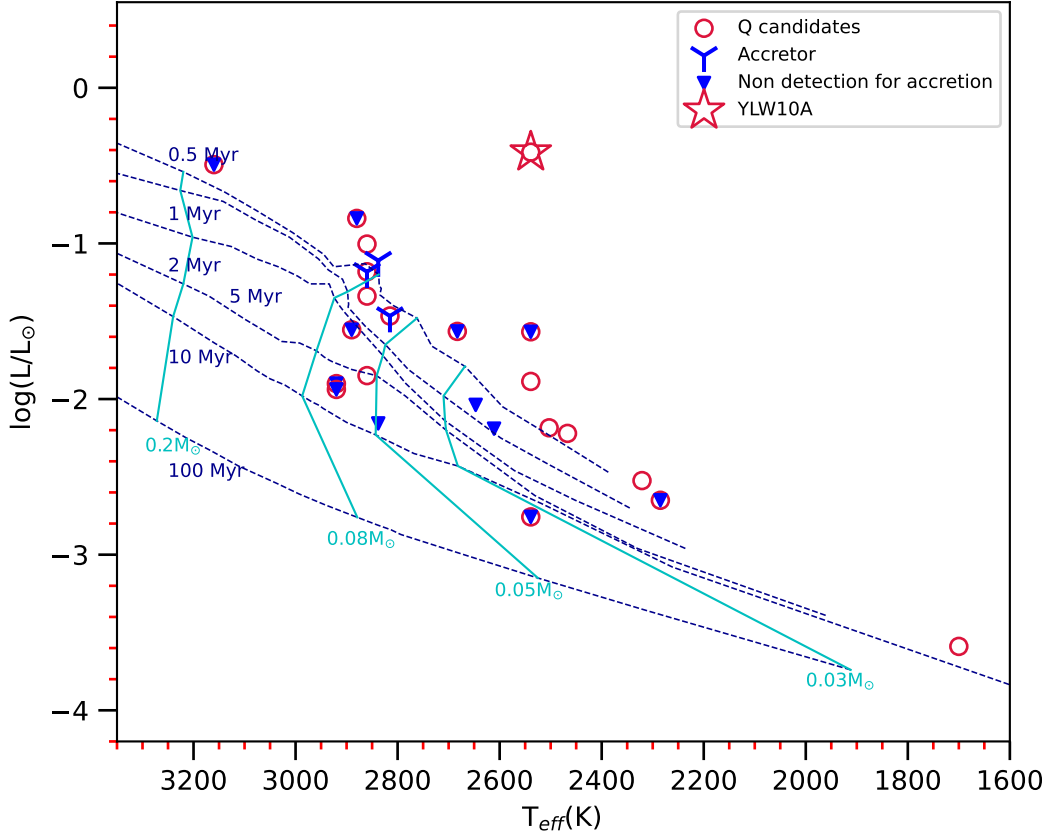


Figure 10. Bolometric luminosity versus effective temperature. The Q candidates are symbolized in red. Those diagnosed as accretors are marked in blue Y, and non-accretors as blue inverted triangles, as per our observations or from the literature. The mass tracks (in cyan) and isochrones (in blue) from Baraffe et al. (2015) are labelled.

form giant planets, even if planet formation were highly efficient. This has been also pointed out by Payne & Lodato (2007); Liu et al. (2020) based on their simulations using core accretion models of planet formation, and further suggesting that while the formation of Earth like planets around BDs require disk with a few M_J 's, smaller Mars size planets could form in BD disks .

Our Q candidates, primarily of mid-M to mid-L types, exhibit Class II or Class III type disks. This indicates an age less than a few million years, and evolution similar to that of low-mass stars progressing through a pre-main sequence stage. The fraction of disks in the water-bearing sample (on the basis of their SEDs) is $68\% \pm 18\%$. Previous studies have reported a similar disk frequency of $\sim 50\% - 70\%$ for young stars in Ophiore (Jayawardhana et al. 2003; Michel et al. 2021), suggestive of common formation pathway for T-Tauri stars and BDs. More recent studies using comparison of disk fraction of BDs and low mass stars in other star forming regions Damian et al. (2023); Gupta et al. (2024) have also confirmed the BD formation as scaled down version of

low mass star formation. The detection of accretion is limited, though not entirely absent. Out of the 17 sources observed for possible magnetospheric accretion (either with IRTF or VLT), three are found to be accretors. The remaining 14 exhibit no obvious detection, resulting in only upper limits. The detection of accretion also depends upon factors like geometry of disk, sensitivity of our instrument for inherently weak accretors.

In the scenario of substellar formation where a stellar embryo is ejected as a result of dynamical and accretion is terminated, one would expect weak or truncated disks. High fraction of disks in our water-bearing sample suggests, otherwise. Our sample albeit small indicates the presence of disks hence the notion that brown dwarf formation and evolution is a scaled-down version of star formation.

3.3. Notes on Individual Candidates

No. 20 (YLW10A) is previously classified as a young stellar object with notable infrared excess (Young et al. 1986; Dunham et al. 2015), as well as a Chandra X-ray source (Imanishi et al. 2001). Our W-Band data categorizes it as a Q candidate, indicating water absorption at $1.45 \mu\text{m}$. To the best of our knowledge, there is no existing spectroscopic confirmation of this source. To estimate its spectral type, we compared our IRTF spectra with the template stellar spectra of different spectral types from giants to dwarfs in the IRTF SpeX library (Rayner et al. 2009). The templates for previously confirmed young BDs ranging from M6 to M8.5 are utilized from our observations. The spectral typing relies particularly on matching the inverted “V” shape to template spectra, after the best-fit extinction/reddening A_V is accounted. Figure 11 compares the target spectrum with field and young BDs for different spectral types. We deduced an M8 as the best fit, i.e., as a young BD with an extinction of $A_V = 28.6 \text{ mag}$

YLW10A lies away from youngest isochrone presented in Figure 10, i.e., it is too bright as a low-mass M8 BD to be associated with this young cluster at distance of the cluster. In an alternate scenario, it could be a giant that are inherently luminous, especially if placed at a longer distance. Giants/AGBs particularly Mira variables or OH/IR stars also display a peak-like feature in the H band. As AGB stars exhibit strong stellar winds, which upon cooling produce molecules and condense dust making them infrared excess sources, although the excess is typically weaker than produced by young circumstellar dust inherited from the parental molecular cloud. Moreover, the mid-infrared light curves of six years does not indicate any significant variability for this source (Park et al. 2021). We did not find any notable $\text{Br}\gamma$ emission line in our observations that would indicate magnetospheric accretion in this source. We conclude, therefore, that based on the spectral fit, infrared excess, and X-ray detection, YLW10A is most likely to be a part of L1688A, either much younger than other stellar and substellar members or defying a proper isochrone fitting as a consequence of the copious excess emission and excessive extinction. Its position in

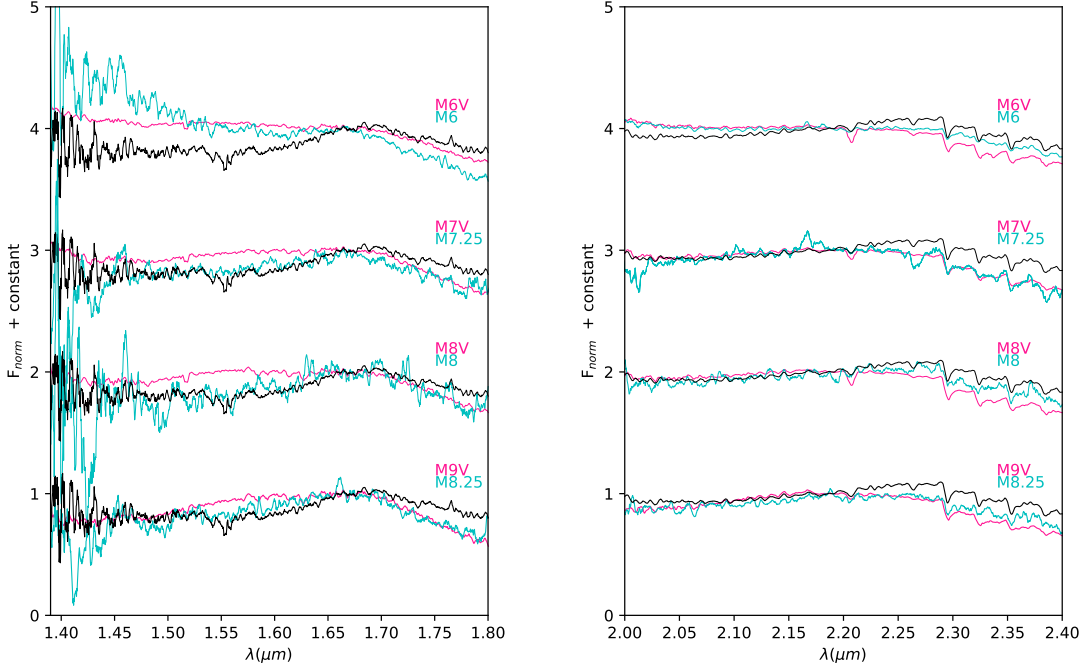


Figure 11. H plus K_s band extinction corrected spectrum of YLW10A, after dereddening by a visual extinction of $A_V = 28.6$ mag. The spectra presented is smoothed to reduce the noise for better visual comparison. The flux is normalised at $1.67 \mu\text{m}$ (H band) and $2.19 \mu\text{m}$ (K_s band), respectively. The field dwarf sequence for mid- to late-M dwarfs is shown in magenta (from the IRTF library), the young BD sequence is shown in cyan (our observations). YLW10A appears to closely resemble the spectral type of M8 in both bands.

the HR diagram and infrared excess may also result from the presence of an unresolved binary companion. Most brown dwarf binaries are quite tightly separated, and likely unresolved with seeing-limited observations. The binarity of YLW10A cannot be confirmed with existing data.

No. 8 is a Q -selected candidate. Our IRTF spectra show a peak in the H band, confirming its nature as a young, cool, and low-gravity object. With an estimated mass of approximately $0.07 M_\odot$, it exhibits signs of magnetospheric accretion. We have detected the presence of the $\text{Br}\gamma$ line, and derived an accretion luminosity of $1.48 \pm 0.13 L_\odot$. The previous estimates using $\text{Pa}\beta$ are $-1.76 L_\odot$ (Natta et al. 2006), and $-1.80 L_\odot$ (Manara et al. 2015). While $\text{Pa}\beta$ may be optically thick and detectable due to other phenomena such as molecular outflows, the presence of $\text{Br}\gamma$, considered optically thin, provides reliable evidence of its accretion activity.

No. 23 is an M6-type known accretor (Natta et al. 2004, 2006; Gatti et al. 2006). Both $\text{Pa}\beta$ and $\text{Br}\gamma$ are detected in our spectra. We derive an accretion luminosity of $-2.68 \pm 1.04 L_\odot$ (using $\text{Pa}\beta$), and $-1.83 \pm 0.32 L_\odot$ (using $\text{Br}\gamma$). The literature values of the accretion luminosity using $\text{Pa}\beta$ are reported as $-2.87 L_\odot$ (Natta et al. 2006), and

$-3.08 L_{\odot}$ (Manara et al. 2015). Our analysis gives an estimated mass of $\sim 0.08 M_{\odot}$, i.e., at the stellar and substellar mass boundary.

4. CONCLUSIONS

In summary, on-off infrared imaging with a narrow-band filter centered on the 1.45 microns water absorption proves efficient in the selection of objects with cool atmospheres. Unbiased by the presence of disks, this method is particularly sensitive to selection of cool M and L dwarfs. This is in contrast to most surveys (e.g., Spitzer, WISE etc.) targeting young populations in star-forming regions to identify disk candidates based on infrared excess. However, W-band selection has its own limitation, as the criteria may break down in high-extinction environments. Additionally, while it is effective in identifying ultracool dwarfs, there is a degeneracy between spectral types for young BDs and field brown dwarfs. The single detection marker for water-bearing candidates, with checks on membership, leads to a reliable target list for follow-up spectroscopic confirmation. The contribution of this work follows.

1. In the core of the Ophiuchus dark cloud complex, L1688 A, the water-band imaging technique works well as 20 of the 22 candidates turn out to have spectral types ranging from M4 to L4.
2. We conducted a membership analysis to verify association with the known young cluster by constraining their proper motions derived from deep infrared images calibrated with bright Gaia sources, and by evaluating their ages and masses. A total of 21 out of 22 candidates were confirmed to be young members.
3. The high fraction of disks in our sample points towards a substellar formation scenario similar to that for low-mass stars.
4. Eight relatively bright low-mass stars and brown dwarf candidates were observed spectroscopically. In addition to affirming their cool temperatures, we confirmed accretion signatures in two very low-mass objects.
5. Spectroscopic analysis of YLW10A (No. 20) revealed an M8 spectral type. Based on the HR diagram, YLW10A could be a potential unresolved close BD-BD binary candidate.

TS and WPC acknowledge the financial support for this work by the National Science and Technology Council (NSTC) grants 113-2123-M-008-004 and 113-2740-M-008-005.

REFERENCES

- | | |
|--|--|
| <p>Almendros-Abad, V., Manara, C. F., Testi, L., et al. 2024, <i>A&A</i>, 685, A118.
doi:10.1051/0004-6361/202348649</p> | <p>Allers, K. N., Jaffe, D. T., Luhman, K. L., et al. 2007, <i>ApJ</i>, 657, 511.
doi:10.1086/510845</p> |
|--|--|

- Allers, K. N. & Liu, M. C. 2020, *PASP*, 132, 104401.
doi:10.1088/1538-3873/aba811
- Apai, D., Pascucci, I., Bouwman, J., et al. 2005, *Science*, 310, 834.
doi:10.1126/science.1118042
- Bate, M. R. & Bonnell, I. A. 2005, *MNRAS*, 356, 1201.
doi:10.1111/j.1365-2966.2004.08593.x
- Bessell, M. S. & Brett, J. M. 1988, *PASP*, 100, 1134. doi:10.1086/132281
- Bate, M. R. 2012, *MNRAS*, 419, 3115.
doi:10.1111/j.1365-2966.2011.19955.x
- Bonnell, I. A., Clark, P., & Bate, M. R. 2008, *MNRAS*, 389, 1556.
doi:10.1111/j.1365-2966.2008.13679.x
- Burrows, A., Marley, M., Hubbard, W. B., et al. 1997, *ApJ*, 491, 856.
doi:10.1086/305002
- Calvet, N., Muzerolle, J., Briceño, C., et al. 2004, *AJ*, 128, 1294.
doi:10.1086/422733
- Chambers, K. C., Magnier, E. A., Metcalfe, N., et al. 2016, *arXiv:1612.05560*.
doi:10.48550/arXiv.1612.05560
- Chiang, P. & Chen, W. P. 2015, *ApJL*, 811, L16.
doi:10.1088/2041-8205/811/2/L16
- Cieza, L. A., Ruíz-Rodríguez, D., Hales, A., et al. 2019, *MNRAS*, 482, 698.
doi:10.1093/mnras/sty2653
- Cohen, J. G., Frogel, J. A., Persson, S. E., et al. 1981, *ApJ*, 249, 481.
doi:10.1086/159308
- Cushing, M. C., Vacca, W. D., & Rayner, J. T. 2004, *PASP*, 116, 362.
doi:10.1086/382907
- Cutri, R. M., Skrutskie, M. F., van Dyk, S., et al. 2003, *VizieR Online Data Catalog*, 2246. II/246
- Damian, B., Jose, J., Biller, B., et al. 2023, *Journal of Astrophysics and Astronomy*, 44, 77.
doi:10.1007/s12036-023-09968-2
- Damian, B., Jose, J., Biller, B., et al. 2023, *ApJ*, 951, 139.
doi:10.3847/1538-4357/acd115
- Dubber, S., Biller, B., Allers, K., et al. 2021, *MNRAS*, 505, 4215.
doi:10.1093/mnras/stab1397
- Dubber, S., Biller, B., Albert, L., et al. 2023, *MNRAS*, 520, 3383.
doi:10.1093/mnras/stad283
- Esplin, T. L. & Luhman, K. L. 2020, *AJ*, 159, 282.
doi:10.3847/1538-3881/ab8dbd
- Filippazzo, J. C., Rice, E. L., Faherty, J., et al. 2015, *ApJ*, 810, 158.
doi:10.1088/0004-637X/810/2/158
- Dunham, M. M., Allen, L. E., Evans, N. J., et al. 2015, *ApJS*, 220, 11.
doi:10.1088/0067-0049/220/1/11
- Gaia Collaboration 2022, *VizieR Online Data Catalog*, 1355
- Greene, T. P. & Meyer, M. R. 1995, *ApJ*, 450, 233. doi:10.1086/176134
- Günther, H. M., Cody, A. M., Covey, K. R., et al. 2014, *AJ*, 148, 122.
doi:10.1088/0004-6256/148/6/122
- Herschel Point Source Catalogue Working Group, Marton, G., Calzoletti, L., et al. 2020, *VizieR Online Data Catalog*, 8106. VIII/106
- Gupta, S., Jose, J., Das, S. R., et al. 2024, *MNRAS*, 528, 5633.
doi:10.1093/mnras/stae369
- Herczeg, G. J. & Hillenbrand, L. A. 2015, *ApJ*, 808, 23.
doi:10.1088/0004-637X/808/1/23
- Imanishi, K., Koyama, K., & Tsuboi, Y. 2001, *ApJ*, 557, 747. doi:10.1086/321691
- Jose, J., Biller, B. A., Albert, L., et al. 2020, *ApJ*, 892, 122.
doi:10.3847/1538-4357/ab74dd
- Kirkpatrick, J. D., Barman, T. S., Burgasser, A. J., et al. 2006, *ApJ*, 639, 1120. doi:10.1086/499622
- Kumar, S. S. 1963, *ApJ*, 137, 1121.
doi:10.1086/147589
- Lada, C. J., Lada, E. A., Clemens, D. P., et al. 1994, *ApJ*, 429, 694.
doi:10.1086/174354
- Lalchand, B., Chen, W.-P., Biller, B. A., et al. 2022, *AJ*, 164, 125.
doi:10.3847/1538-3881/ac8547
- Loren, R. B. 1989, *ApJ*, 338, 902.
doi:10.1086/167244

- Lucas, P. W., Roche, P. F., Allard, F., et al. 2001, *MNRAS*, 326, 695.
doi:10.1046/j.1365-8711.2001.04666.x
- Luhman, K. L., Peterson, D. E., & Megeath, S. T. 2004, *ApJ*, 617, 565.
doi:10.1086/425228
- Luhman, K. L. & Rieke, G. H. 1999, *ApJ*, 525, 440. doi:10.1086/307891
- McClure, M. K., Furlan, E., Manoj, P., et al. 2010, *ApJS*, 188, 75.
doi:10.1088/0067-0049/188/1/75
- Meyer, M. R., Calvet, N., & Hillenbrand, L. A. 1997, *AJ*, 114, 288.
doi:10.1086/118474
- Ortiz-León, G. N., Loinard, L., Kounkel, M. A., et al. 2017, *ApJ*, 834, 141.
doi:10.3847/1538-4357/834/2/141
- Ngoc, P. B. 2022, *Communications in Physics*, 32, 95.
doi:10.15625/0868-3166/16258
- Michel, A., van der Marel, N., & Matthews, B. C. 2021, *ApJ*, 921, 72.
doi:10.3847/1538-4357/ac1bbb
- Ngoc, P. B. 2022, *Communications in Physics*, 32, 95.
doi:10.15625/0868-3166/16258
- Payne, M. J. & Lodato, G. 2007, *MNRAS*, 381, 1597.
doi:10.1111/j.1365-2966.2007.12362.x
- Padoan, P. & Nordlund, Å. 2002, *ApJ*, 576, 870. doi:10.1086/341790
- Park, W., Lee, J.-E., Contreras Peña, C., et al. 2021, *ApJ*, 920, 132.
doi:10.3847/1538-4357/ac1745
- Payne, M. J. & Lodato, G. 2007, *MNRAS*, 381, 1597.
doi:10.1111/j.1365-2966.2007.12362.x
- Puget, P., Stadler, E., Doyon, R., et al. 2004, *Proc. SPIE*, 5492, 978.
doi:10.1117/12.551097
- Rayner, J. T., Cushing, M. C., & Vacca, W. D. 2009, *ApJS*, 185, 289.
doi:10.1088/0067-0049/185/2/289
- Rayner, J. T., Toomey, D. W., Onaka, P. M., et al. 2003, *PASP*, 115, 362.
doi:10.1086/367745
- Wilking, B. A., Gagné, M., & Allen, L. E. 2008, *Handbook of Star Forming Regions*, Volume II, 351.
doi:10.48550/arXiv.0811.0005
- Reipurth, B. & Clarke, C. 2001, *AJ*, 122, 432. doi:10.1086/321121
- Scholz, A. & Jayawardhana, R. 2008, *ApJL*, 672, L49. doi:10.1086/526340
- Vacca, W. D., Cushing, M. C., & Rayner, J. T. 2003, *PASP*, 115, 389.
doi:10.1086/346193
- Young, E. T., Lada, C. J., & Wilking, B. A. 1986, *ApJL*, 304, L45.
doi:10.1086/184668
- Whitworth, A. P. & Stamatellos, D. 2006, *A&A*, 458, 817.
doi:10.1051/0004-6361:20065806
- Jayawardhana, R., Ardila, D. R., Stelzer, B., et al. 2003, *AJ*, 126, 1515.
doi:10.1086/377144
- Natta, A., Testi, L., Muzerolle, J., et al. 2004, *A&A*, 424, 603.
doi:10.1051/0004-6361:20040356
- Manara, C. F., Testi, L., Natta, A., et al. 2015, *A&A*, 579, A66.
doi:10.1051/0004-6361/201526169
- Alcalá, J. M., Manara, C. F., Natta, A., et al. 2017, *A&A*, 600, A20.
doi:10.1051/0004-6361/201629929
- Ladjelate, B., André, P., Könyves, V., et al. 2020, *A&A*, 638, A74.
doi:10.1051/0004-6361/201936442
- Zucker, C., Speagle, J. S., Schlafly, E. F., et al. 2020, *A&A*, 633, A51.
doi:10.1051/0004-6361/201936145
- Ducourant, C., Teixeira, R., Krone-Martins, A., et al. 2017, *A&A*, 597, A90.
doi:10.1051/0004-6361/201527574
- Alves de Oliveira, C., Moraux, E., Bouvier, J., et al. 2010, *A&A*, 515, A75.
doi:10.1051/0004-6361/200913900
- Erickson, K. L., Wilking, B. A., Meyer, M. R., et al. 2011, *AJ*, 142, 140.
doi:10.1088/0004-6256/142/4/140
- Natta, A., Testi, L., Muzerolle, J., et al. 2004, *A&A*, 424, 603.
doi:10.1051/0004-6361:20040356
- Testi, L., Natta, A., Scholz, A., et al. 2016, *A&A*, 593, A111.
doi:10.1051/0004-6361/201628623
- Fitzpatrick, E. L. 1999, *PASP*, 111, 63.
doi:10.1086/316293

- Bertin, E. & Arnouts, S. 1996, *A&AS*, 117, 393. doi:10.1051/aas:1996164
- Grasser, N., Ratzenböck, S., Alves, J., et al. 2021, *A&A*, 652, A2. doi:10.1051/0004-6361/202140438
- Robitaille, T. P. 2017, *A&A*, 600, A11. doi:10.1051/0004-6361/201425486
- Gatti, T., Testi, L., Natta, A., et al. 2006, *A&A*, 460, 547. doi:10.1051/0004-6361:20066095
- Testi, L., Natta, A., Scholz, A., et al. 2016, *A&A*, 593, A111. doi:10.1051/0004-6361/201628623
- Natta, A., Testi, L., & Randich, S. 2006, *A&A*, 452, 245. doi:10.1051/0004-6361:20054706
- Betti, S. K., Follette, K. B., Ward-Duong, K., et al. 2023, *AJ*, 166, 262. doi:10.3847/1538-3881/ad06b8
- Allen, M. G., Ochsenbein, F., Derriere, S., et al. 2014, *Astronomical Data Analysis Software and Systems XXIII*, 485, 219
- Gunther, H. M., Cody, A. M., Covey, K. R., et al. 2014, *VizieR Online Data Catalog*, 514
- Cutri, R. M. & et al. 2012, *VizieR Online Data Catalog*, 2311. II/311
- Almendros-Abad, V., Manara, C. F., Testi, L., et al. 2024, *A&A*, 685, A118. doi:10.1051/0004-6361/202348649
- Testi, L., Natta, A., Manara, C. F., et al. 2022, *A&A*, 663, A98. doi:10.1051/0004-6361/202141380
- Liu, B., Lambrechts, M., Johansen, A., et al. 2020, *A&A*, 638, A88. doi:10.1051/0004-6361/202037720
- Baraffe, I., Homeier, D., Allard, F., et al. 2015, *A&A*, 577, A42. doi:10.1051/0004-6361/201425481